Scaling Effects on Side Load Generation in Subscale Rocket Nozzles

R. Stark* and C. Génin†

German Aerospace Center (DLR), Lampoldshausen, D-74239, Germany

During the start-up of a rocket engine at sea-level, the flow will separate inside the supersonic part of the nozzle. The separated nozzle flow generates significant side loads which may damage the nozzle, the thrust chamber and the thrust vector control system. To study the effect of scaling the size of the nozzle, the DLR institute of space propulsion carried out a cold flow test campaign with two rocket nozzles of different sizes. The experimental data confirm the expected trend.

Nomenclature

c_e	averaged exit velocity, m/s
d	diameter, mm
k	scaling factor
l	length, mm
p	pressure, MPa
t	time, s
F	thrust, force, N
R	radius, mm
Re_s	Reynolds number along nozzle wall
Ma	Mach number
X	axial position, mm
$\dot{m}$	mass flow rate, kg/s
τ	torque, Nm
NPR	nozzle pressure ratio, $p_\mathrm{cc}/p_\mathrm{a}$, p_0/p_a
Subscript	
0	total condition
1	initial nozzle
2	scaled nozzle
a	ambient
af	attached flow
bf	back flow
cc	combustion chamber
e	exit
la	lever arm
p	plateau
sep	separation
t	throat
w	wall
D	design
SL	side load

*Head of Group Fluid Flows, Department of Rocket Propulsion.

†Research Scientist, Department of Rocket Propulsion.

I. Introduction

During the transient start-up and shutdown of a rocket engine, the flow inside a convergent-divergent nozzle can only achieve a certain degree of overexpansion. Beyond that threshold, the boundary layer lifts off and separates from the wall, which allows ambient air to be sucked into the remaining back flow section of the nozzle (Fig. 1). The unsteady nature and circumferentially asymmetric distribution of the flow separation generates an significant side load, as the pressure difference between opposing nozzle walls result in a force acting with a lever arm about the rocket engine's cardan point. The increasing NPR (NPR = p_{cc}/p_a or p_0/p_a) shifts the separation position towards the nozzle exit. The side load increases, as its magnitude is a function of the separation position, and the size of the nozzle. The maximum side load amplitude occurs as the Mach disc passes the nozzle exit cross section[1].

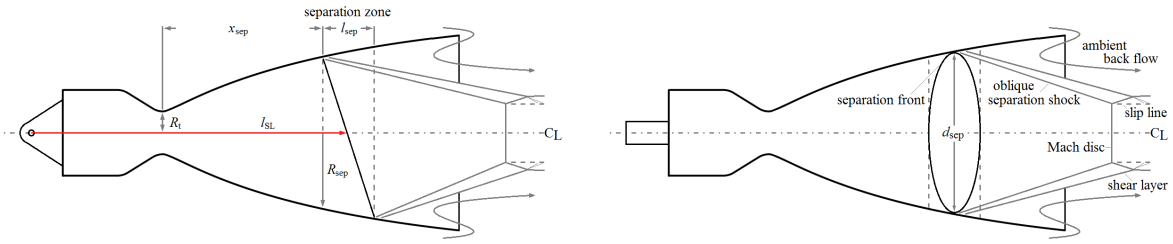

Figure 1. Topology of separated nozzle flow. Side view (left) and top view (right).

The basic process of side load generation[2–4] can be superimposed by events like the ignition burst peak, a partially reattached flow caused by boundary layer transition[1,5], or a transition from a free shock separation (FSS) to a restricted shock separation (RSS) and vice versa in parabolic contoured nozzles[6] (TOP). This flow characteristic and the resulting side loads were observed for the J-2S rocket engine by Nave and Coffey[7]. Terhardt et al.[8] identified a comparable behavior for the European main stage rocket engine Vulcain. Detailed studies on side load generation in TOP nozzles followed in Europe[9–11], Japan[12], and the United States[13–15].

Increased side loads affect the nozzle structure integrity, the engine, the thrust vector control system (TVCS), the rocket stages and the payload. For this reason, side load prediction is of particular interest. Models based on wall pressure pulsation and its statistical distribution were suggested by Dumnov[16] (RD-0120) and Terhardt et al.[17]. Vuillermoz et al.[18] presented the Vulcain 2 design and estimated the side loads using the method proposed by Schmucker[19]. Although side loads in rocket nozzles cannot be avoided, a successful prediction will still enable lighter nozzles, thrust chambers and TVCSs. A reduced load transmission will especially profit the future application of lightweight electrical driven engine TVCS.

To generate side load model validation data, the DLR institute of space propulsion performed tests with different subscale nozzles[20,21] and side load reduction devices[22,23]. To study the effect of nozzle scaling, two nozzles of identical inner norm contour, but with different sizes were tested and the results are presented.

A. Side load generation

The side load force F_{SL} of rocket nozzles is generated by the pressure differences on opposite sides of the nozzle wall. It can be subdivided into four parts: the attached nozzle flow F_{SLaf}, the separation zone F_{SLsep}, the back flow F_{SLbf}, and the ambient flow F_{SLa}.

$$F_{SL} = F_{SLaf} + F_{SLsep} + F_{SLbf} + F_{SLa} \tag{1}$$

During transient operation the separation zone and the back flow are the main drivers of side load generation. The separation zone is defined upstream by the incipient separation, where the lowest undisturbed wall pressure p_{sep} can be detected, and downstream by the plateau pressure $p_p \approx 0.9 \cdot p_a$, from which on only back flow values are present. Figure 2 (left) illustrates how both positions can be determined by the response of a wall pressure signal on a separation zone, passing due to a slowly increasing NPR. Initially a constant back flow value is present. As the downstream border of the separation zone starts passing the port, the wall

pressure drops and its fluctuations increase. A period of huge wall pressure fluctuations follows, indicating the separation shock system hitting the port position. The temporarily attached flow is represented by attaining the minimal wall pressure value. If the wall pressure peaks fail to appear any further, the attached flow state is then proved to be fully developed and the incipient separation has passed the port.

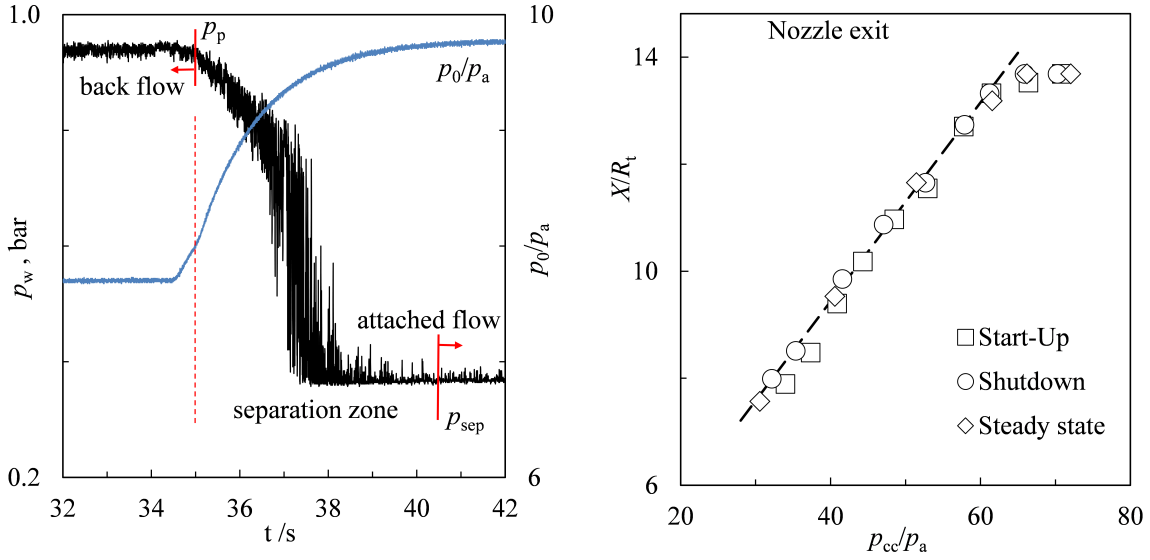

Figure 2. Separation zone passing a pressure port (left) and separation position as function of NPR (right).

The fluctuation magnitude illustrates the pressure difference on opposite nozzle walls Δp_{wsep} which causes the side load. The length of the separation zone l_{sep} and its diameter d_{sep} is related to the side load such as:

$$F_{SLsep} \approx l_{sep} \cdot d_{sep} \cdot \Delta p_{wsep} \tag{2}$$

Once the nozzle flows full, the back flow part F_{SLbf} becomes Zero and the separation zone part F_{SLsep} along with its length l_{sep} is reduced due to the increase in NPR[1,24]. Additionally, the pressure difference Δp_{wsep} also decreases and the diameter d_{sep} approaches the nozzle exit diameter d_e. Figure 2 (right) illustrates the evolution of the separation position within the nozzle of a LOX/GH2 rocket engine[24]. The separation zone reaches the nozzle exit for a combustion chamber pressure of $p_{cc} \approx 6$ MPa. If the combustion chamber pressure is furthermore increased, the separation position deviates from linear trend as it approaches the nozzle exit, shaping into a hockey stick.

During ascent of a launcher, the separation zone disappears and the ambient pressure fluctuations become the main driver of side load generation (e.g. buffeting loads).

The side loads induced by the attached flow F_{SLaf} are the lowest part of the overall load as the fluctuation of the wall pressure is in the range of $\Delta p_{waf} \approx 1\%$. They result from combustion roughness, which is mainly dependent on the quality of the combustion chamber. If significant combustion instabilities occur during transient engine start-up, this loads cannot be ignored.

B. Side load scaling

The separation zone length l_{sep}, diameter d_{sep}, and position X_{sep} are dependant on the NPR and the nozzle contour[24]. Scaling the contour ($R_{t2} = k \cdot R_{t1}$) scales the geometrical parameters by the same order (Eq. (3)).

$$l_{sep} = f(NPR, R_t) \approx 0.45 \cdot R_{sep} \ , \ d_{sep} = f(NPR, R_t) \approx 2 \cdot R_{sep} \ , \ X_{sep} = f(NPR, R_t) \ , \ R_{t2} = k \cdot R_{t1} \tag{3}$$

As the flow pattern is scaled up, but the pressure difference remains ($\Delta p_{wsep2} = \Delta p_{wsep1}$, Eq. (4)), the overall side load F_{SL} is expected to scale quadratically (Eq. (5)).

$$F_{SLsep2} \approx k \cdot l_{sep1} \cdot k \cdot d_{sep1} \cdot \Delta p_{wsep1} \tag{4}$$

$$F_{SLsep2} = k^2 \cdot F_{SLsep1} \Rightarrow F_{SL2} \approx k^2 \cdot F_{SL1} \tag{5}$$

The thrust of a rocket engine F is a function of its total mass flow rate $\dot{m}$ and the average exhaust velocity c_e. As $\dot{m}$ is a function of the throat radius R_t, the thrust scales quadratically as well (Eq. 6)). Hence, the side load to thrust ratio is expected to remain constant (Eq. (7)).

$$F = \dot{m} \cdot c_e \ , \ \dot{m} = f(p_{cc}, R_t^2) \ , \ F_2 = k^2 \cdot F_1 \tag{6}$$

$$\frac{F_{SL1}}{F_1} = \frac{F_{SL2}}{F_2} = const \tag{7}$$

The loading on the TVCS is the product of the overall side load F_{SL} and the lever arm l_{SL} (Eq. (8), Fig. 1), which is expressed as side load torque τ_{SL}. Consequently, scaling the complete rocket engine leads to a first attempt at a cubically scaling side load torque (Eq. (9)). This is valid for lever arms starting at the nozzle throat. But as a matter of fact, the combustion chamber will be scaled in its diameter and not necessarily in its length, as the length is a result of the combustion process that remains the same. In contrast to the side load, the ratio of the induced side load torque and thrust scales linearly with the factor $(c + k)/(c + 1)$ (Eq. (10)).

$$\tau_{SLsep} = l_{SL} \cdot F_{SLsep} \quad \Rightarrow \quad \tau_{SLsep2} = k \cdot l_{SL} \cdot k^2 \cdot F_{SLsep1} \tag{8}$$

$$\tau_{SL2} = k^3 \cdot \tau_{SL1} \quad \Rightarrow \quad \tau_{SL2} = \frac{c+k}{c+1} \cdot k^2 \cdot \tau_{SL1} \tag{9}$$

$$\frac{\tau_{SL2}}{F_2} = \frac{c+k}{c+1} \cdot \frac{\tau_{SL1}}{F_1} \ , \ \neq const \tag{10}$$

II. Experimental Setup

The experimental study was conducted at DLR's cold flow subscale test facility P6.2 in Lampoldshausen. Figure 3 shows a sketch of the assembly, with its 20 MPa vessels on the left, where dry gaseous nitrogen is stored under ambient temperature. A line system, including automatic valves, filters, pressure reducers, regulation valves, and mass flow meters, connects the supply storage with the settling chambers, mounted vertically at the top of the high-altitude chamber (middle) or horizontally at the test rig (right). A third facility setup offers an additional ejector system to decouple the high-altitude chamber pressure from the test specimen's mass flow rate (bottom left). To reduce turbulence, the settling chambers are equipped with a set of grids and honeycombs. The presented study was performed under ambient conditions using the horizontal test rig.

The facility features total pressures up to 6 MPa and mass flow rates up to 4.2 kg/s. Dry gaseous nitrogen is used as working fluid to avoid condensation effects (H2O, CO2, O2, etc.). The nitrogen flow passes a settling chamber, a cross-section constriction, and a bending tube before it accelerates through the convergent-divergent nozzle (Fig. 3, right).

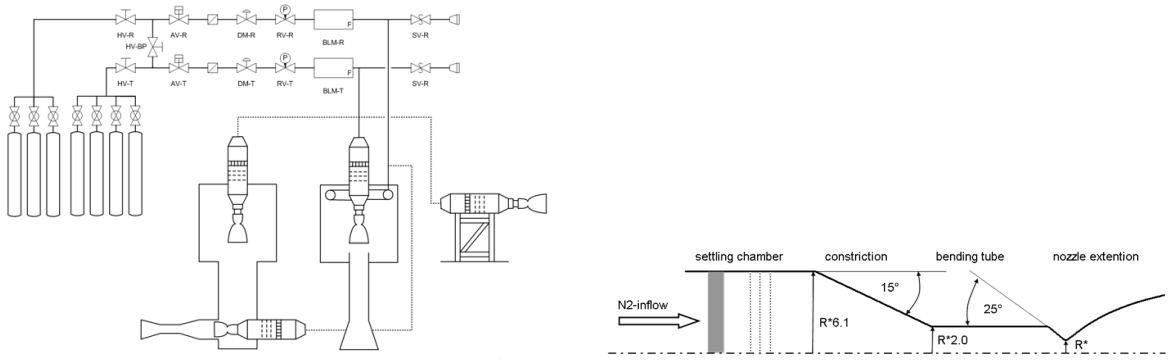

Figure 3. Test facility P6.2. Assembly (left) and nozzle feeding system (right).

A. Side load measurement

The side loads were measured using a thin-walled bending tube mounted upstream the subsonic nozzle inflow (Fig. 4, left). An asymmetric pressure distribution inside the nozzle causes a force perpendicular to the nozzle symmetry axis which bends the tube. The resulting bending stress is proportional to the load and it is measured using strain gauges (SG). A force component is determined by pairs of gauges connected as a full Wheatstone bridge (Fig. 4, right). The wiring configuration, connecting opposite branches of the bridge, and the positioning assure that tensile, torsional and temperature stresses are compensated for and only bending stresses detune the Wheatstone bridge.

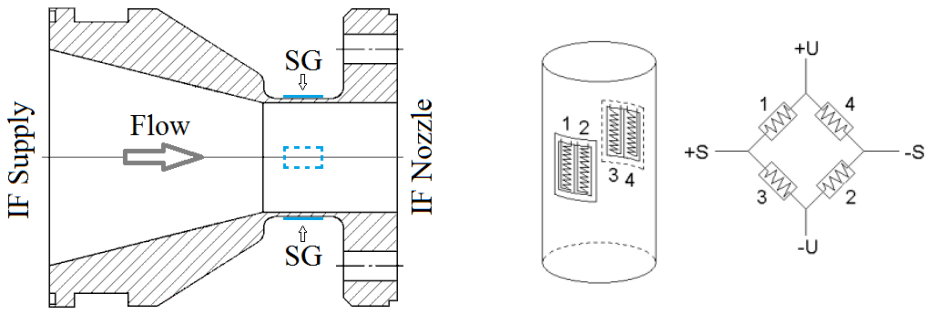

Figure 4. Side load measurement device (left) and strain gauges configuration (right).

The bridges were calibrated with different weights fixed at the nozzle exit (Fig. 5, right). Releasing a weight by cutting its holding string yields the static and the dynamic response of the system such as the eigenfrequency and rate of damping (Fig. 5, left). With the resulting characteristics, the measured voltage signals can be recalculated as forces acting at the end of the nozzle.

The side load measurement device (SLMD) is equipped with two perpendicular arranged bridges. All side load data were recorded with a frequency of 25 kHz and a signal filter of 8 kHz.

B. Nozzle designs and pressure measurement

For the purpose of this study a truncated ideal contour (TIC) nozzle was designed. The nozzle features a design Mach number of $Ma_D = 4.8$ and a throat radius of $R_t = 10$ mm. It was truncated to a length allowing full flowing condition at a nozzle pressure ratio of NPR = 50, leading to a wall exit Mach number of $Ma_e = 4.25$. This initial specimen was designated as TIC-2048. Its contour was scaled up with a factor of $k = 1.5$, leading to a throat radius of $R_t = 15$ mm. The resulting second specimen was designated as

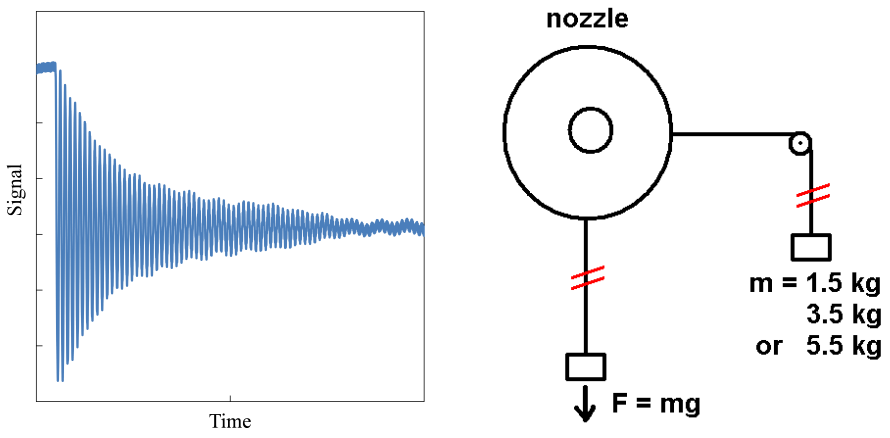

Figure 5. SLMD calibration. Typical calibration signal (left) and weight application (right).

TIC-3048. Both specimens were made of acrylic glass with a wall thickness of 8 mm. The main nozzle design parameters are given in table 1.

Table 1. Design parameters of TIC nozzles

		TIC-2048/TIC-3048
Design Mach number	Ma_{D}	4.8
Exit wall mach number	Ma_{e}	4.25
Divergent Length	l_{div} , $(1/R_{\mathrm{t}})$	13.8
Exit wall angle	α_e , (deg)	4.9
Area ratio	$\epsilon = A_{\mathrm{e}}/A_{\mathrm{t}}$	17.0
Nozzle throath radius	R_{t} , (mm)	10.0/15.0

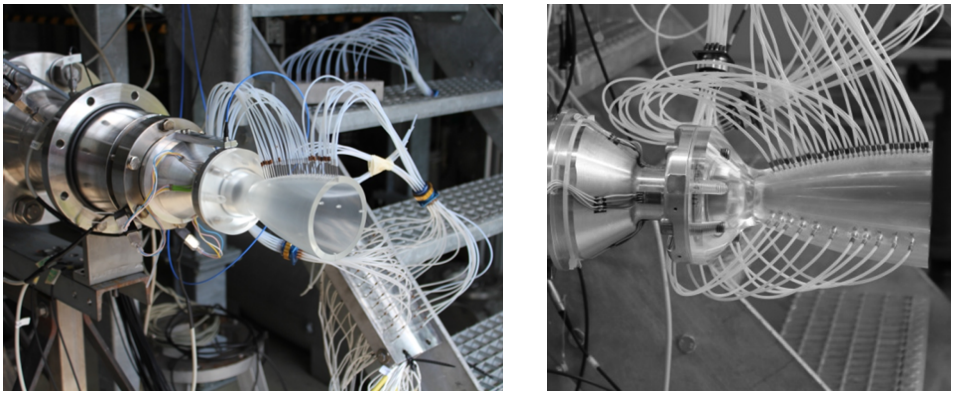

Figure 6. Mounted nozzles. TIC-3048 (left) and TIC-2048 (right).

The nozzles TIC-2048 and TIC-3048 were equipped with axial rows of pressure ports, featuring a constant axial spacing of 4 mm and 6 mm, respectively. The static wall pressures were measured via 0.5 mm orifices, drilled perpendicular into the nozzle wall. These orifices were connected with small metal pipes and Teflon tubes (Fig. 6) to collecting blocks where piezo-resistive Kulite XT-154-190M absolute pressure transducers were screwed into. The transducers had a measurement range of 0.1 MPa with an accuracy of 0.5%, relative to the upper range limit. The natural frequency of the transducers pressure sensitive semiconductor membrane

is higher than 50 kHz; however, due to the low eigenfrequency of the Teflon tubes, the pressure signals were filtered with a cut-off frequency of 160 Hz and recorded with a frequency rate of 1 kHz.

C. Test sequences

All tests were conducted with the same NPR sequences. Figure 7 illustrates the test sequences with its up and down ramping gradients of $d\mathrm{NPR}/dt = \pm 3.4\ s^{-1}$ and $d\mathrm{NPR}/dt = \pm 2\ s^{-1}$, respectively. Every specimen was tested at least three times for validation.

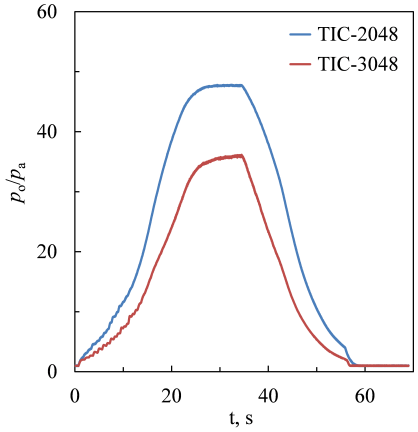

Figure 7. Example of the test sequences.

III. Results and discussion

As the flow characteristics of both nozzles remain the same, the separation position X_{sep} and the related separation zone diameter d_{sep} will scale with the factor k (Eq. (4)). The question is whether the separation zone length l_{sep} also scales with k as expected.

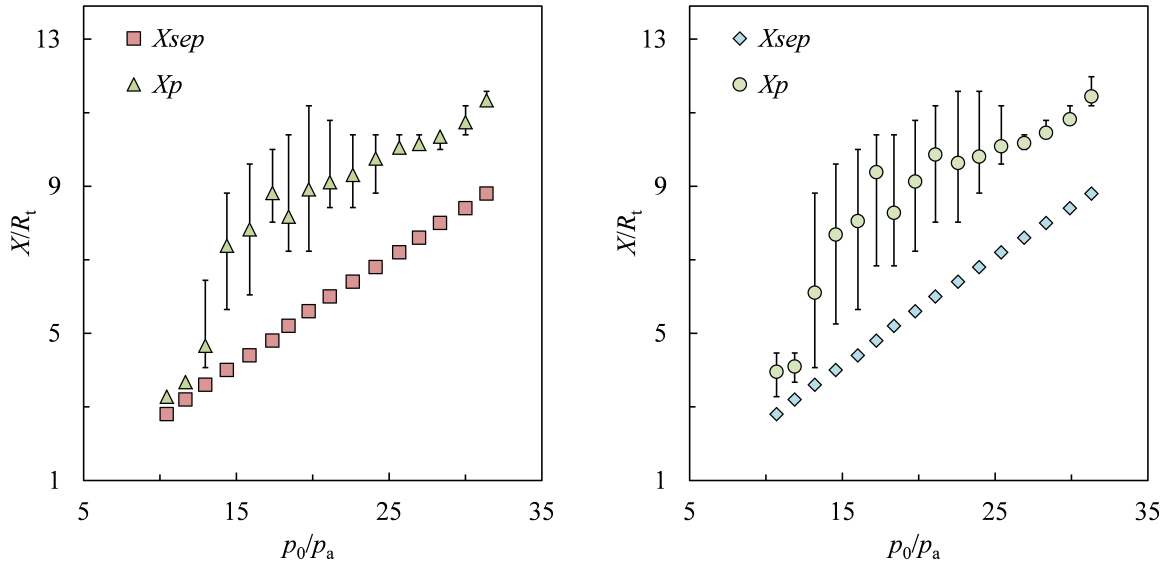

Figure 8. Position of the separation zone. TIC-2048 (left) and TIC-3048 (right).

Figure 8 compares the separation characteristics of the initial nozzle TIC-2048 (left) and the scaled nozzle TIC-3048 (right). The up- and downstream border of the separation zone, X_{sep} and X_p, were determined as described in section (A). The data sets represent the averaged values of all tests. The determination of the incipient separation position X_{sep} is well defined and its variance is little. Hence, the variance is covered by the size of the used symbols. In contrast, the determination of the downstream border X_p leads to a clear variance due to the heavy wall pressure fluctuations (Fig. 2, left). The incipient separation positions X_{sep} are the same and follow the expected linear trend. Also the plateau pressure positions X_p are comparable. Both nozzles depict an increased variance of X_p for a NPR (p_0/p_a) range of 13-26.

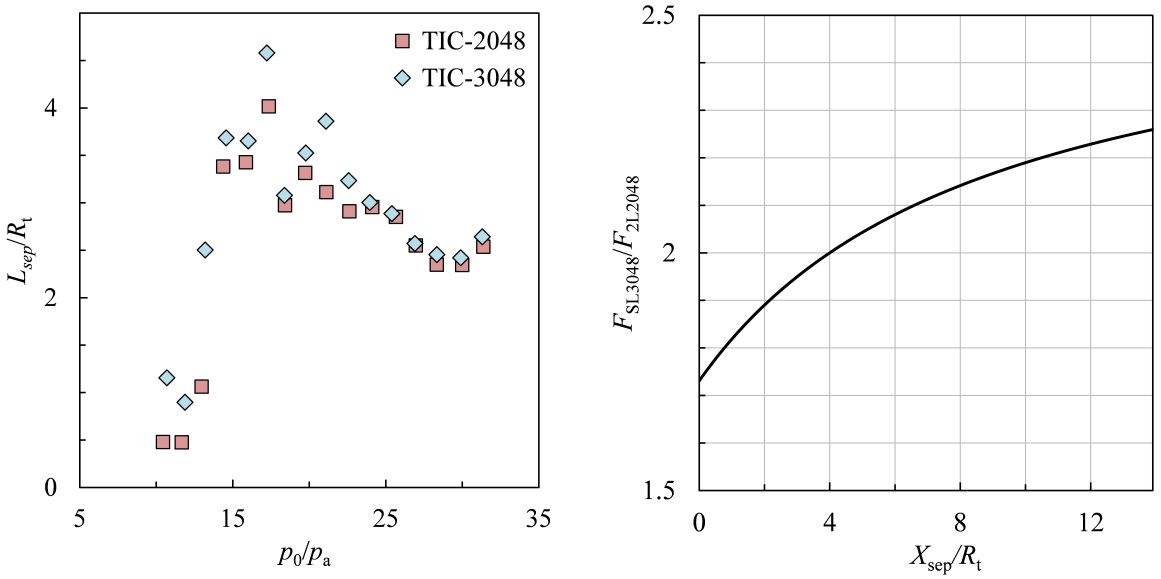

Figure 9. Comparison of separation lengths (left). Expected side load scaling (right).

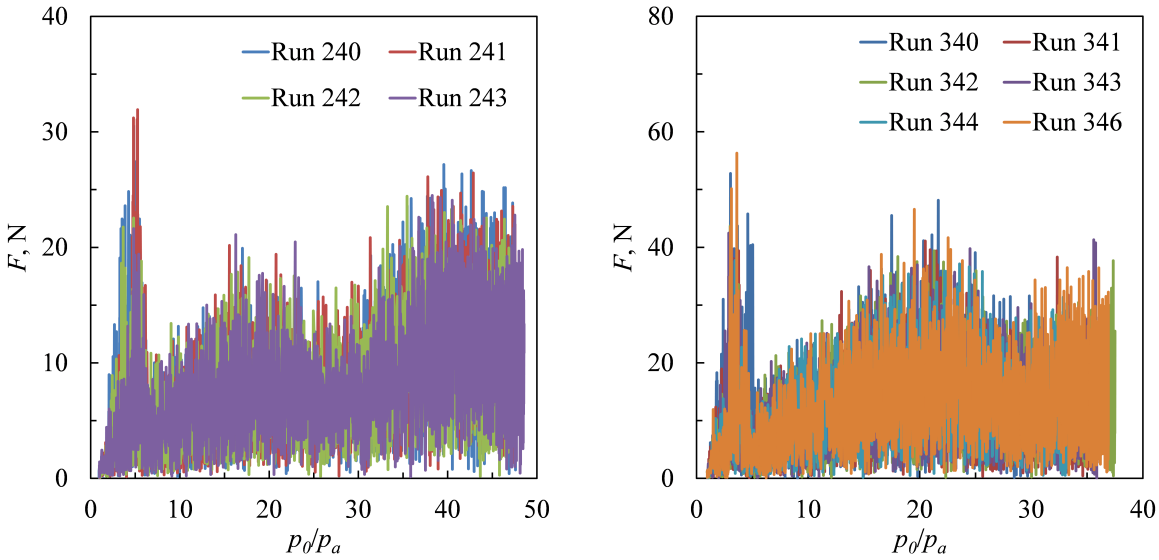

Figure 10. Side loads as function of the NPR. TIC-2048 (left) and TIC-3048 (right).

Figure 9 (left) gives the comparison of the resulting separation lengths $L_{sep} = X_p - X_{sep}$. The lengths are normalized by the related nozzle throat radii R_{t1} and $R_{t2} = k \cdot R_{t1}$. The separation length scales with

the factor k, as predicted. There might be a slight effect of the NPR gradient $d\text{NPR}/dt$ on the separation length L_{sep}, as the separation shift of the TIC-2048 nozzle happens faster (see section (C)). However, the data are not sufficient for an evident conclusion.

Figure 10 illustrates the repeatability of the side load measurements. The data of TIC-2048 (left) and TIC-3048 (right) are displayed as a function of the NPR. The NPR range of TIC-3048 is narrowed, as no full flowing nozzle was achieved. The side load peaks for NPRs of approximately 3-6 represent a partially reattached flow which is caused by the aforementioned asymmetrical transition from a relaminarized to a turbulent boundary layer separation[1].

It was initially expected that the side loads increase with increasing NPR; however, the loads actually decrease for NPR > 18, before they increase again for NPR > 30. This behavior correlates with the length of the separation zone as shown in Fig. 11 (left), where the averaged values are compared with the related side loads of a single TIC-2048 test run. This behavior only distinctly appears if the amplifying resonance frequency (see section (A)) of the side load measurement device is removed by applying an appropriate transfer function.

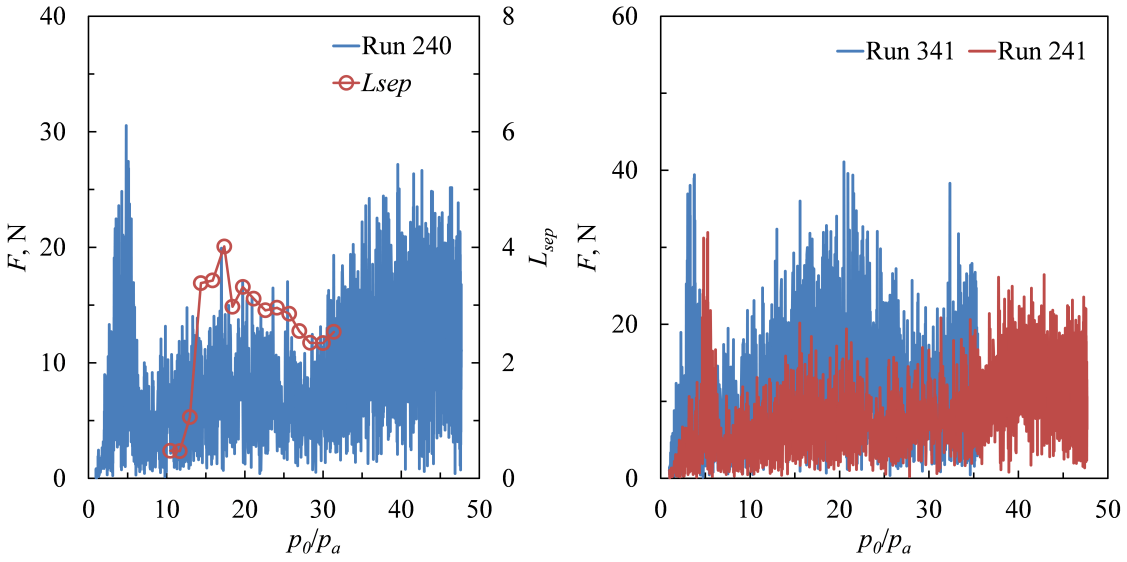

Figure 11. Side loads and separation zone length (left). TIC-2048 and TIC-3048 (right).

Figure 11 (right) compares the side loads of a single TIC-2048 and a single TIC-3048 test run. For TIC-3048, the partial reattached flow appears for lower NPR. As the causal boundary layer transition is a function of the related Reynolds number Re_s along the nozzle wall, its position is shifted upstream for an upscaled nozzle and will be passed for a lower NPR.

As a matter of fact, using a bending tube, the side loads are measured as torques and the derived signals are interpreted as an equivalent force acting at the nozzle exit. As only the divergent part of the nozzle is scaled up, the different lever arms acting about the bending tube have to be taken into account. Figure 9 (right) displays the resulting side load ratio F_{SL3048}/F_{SL2048} as a function of the separation position X_{sep}. The side loads in the NPR range of 10-32 were expected to scale with the factor $F_{SL3048}/F_{SL2048} = 1.97\text{-}2.2$, respectively. The comparison given in Fig. 11 (right) illustrate the successful prediction.

IV. Conclusion

It could be shown that the separation zone length l_{sep} scales with the geometrical factor k. Hence, the ratio of side load and thrust F_{SL}/F remains constant as predicted. However, the side load torque τ_{SL} acting about the nozzle throat scales up linearly with the factor k and has to be considered. A strong deviation of the separation length scale was observed for both nozzles, resulting in an temporarily side load increase. This effect needs future attention to be adapted into side load generation models.

Acknowledgments

The authors like to thank T. Aichner, M. Frey, A. Garus and K. Makowka (all Airbus Safran Launchers GmbH) for fruitful cooperation within the framework of the German national research initiative Propulsion 2020.

References

[1]Stark, R. and Wagner, B., *Experimental study of boundary layer separation in truncated ideal contour nozzles*, Shock Waves, Vol. 19, No. 3, pp. 185-191, 2009.

[2]Frey, M. and Hagemann, G., *Flow separation and side-loads in rocket nozzles*, AIAA-1999-2815, 35th AIAA/ASME/SAE/ASEE Joint Propulsion Conference and Exhibit, Los Angeles, CA, June 20-24, 1999.

[3]Hagemann, G., Frey, M. and Koschel, W., *Appearance of Restricted Shock Separation in Rocket Nozzles*, Journal of Propulsion and Power, Vol. 18, No. 3, pp. 577-584, 2002.

[4]Östlund, J., Damgaard, T. and Frey, M., *Side-Load Phenomena in Highly Overexpanded Rocket Nozzles*, Journal of Propulsion and Power, Vol. 20, No. 4, pp. 695-704, 2004.

[5]Lawrence, R. A., *Symmetrical and Unsymmetrical Flow Separation in Supersonic Nozzles*, NASA CR 92587, Ph.D. Thesis, Institute of Technology of Southern Methodist University, Dallas, Texas, April 5th, 1967.

[6]Frey, M. and Hagemann, G., *Restricted Shock Separation in Rocket Nozzles*, Journal of Propulsion and Power, Vol. 16, No. 3, 2000, pp. 478-484, 2000.

[7]Nave, L. and Coffey, G., *Sea Level Side Loads in High-Area-Ratio Rocket Engines*, AIAA 1973-1284, 9th Propulsion Conference, Las Vegas, NV, November 5-7, 1973.

[8]Terhardt, M., Hagemann, G. and Frey, M., *Flow Separation and Side-Load Behavior of the Vulcain Engine*, AIAA 1999-2762, 35th Joint Propulsion Conference, Los Angeles, CA, June 20-24, 1999.

[9]Mattsson, J., Högman, U. and Torngren, L., *A Subscale Test Programme on Investigation of Flow Separation and Side-Loads in Rocket Nozzles*, Proceedings of the 3rd European Symposium On Aerothermodynamics of Space Vehicles, ESA SP-426, pp. 373-378, 1998.

[10]Nguyen, A., Deniau, H., Girard, S. and Alizary de Roquefort, T., *Unsteadiness of Flow Separation and End-Effects Regime in a Thrust-Optimized Contour Rocket Nozzle*, Flow, Turbulence and Combustion, Vol. 71, pp. 161-181, 2003.

[11]Verma, S. and Haidn, O., *Study of Restricted Shock Separation Phenomena in a Thrust Optimized Parabolic Nozzle*, Journal of Propulsion and Power, Vol. 25, No. 5, pp. 1046-1057, 2009.

[12]Tomita, T., Takahashi, M., Sasaki, M., Sakamoto, H., Takahashi, M. and Tamura, H., *Experimental evaluation of side-loads in LE-7A prototype engine nozzle*, Shock Waves, Vol. 19, No. 3, pp. 213-228, 2009.

[13]Ruf, J., McDaniels, D. and Brown, A., *Nozzle Side Load Testing and Analysis at Marshall Space Flight Center*, AIAA 2009-4856, 45th Joint Propulsion Conference, Denver, CO, August 2-5, 2009.

[14]Ruf, J., McDaniels, D. and Brown, A., *Details of Side Load Test Data and Analysis for a Truncated Ideal Contour Nozzle and a Parabolic Contour Nozzle*, AIAA 2010-6813 , 46th Joint Propulsion Conference, Nashville, TN, July 26-28, 2010.

[15]Baars, W., Tinney, C., Ruf, J., Brown, A. and McDaniels, D., *Wall Pressure Unsteadiness and Side Loads in Overexpanded Rocket Nozzles*, AIAA Journal, Vol. 50, No. 1, pp. 61-73, 2012.

[16]Dumnov, D., *Unsteady side-load acting on the nozzle with developed separation zone*, AIAA 1996-2815, 32nd Joint Propulsion Conference, Lake Buena Vista, FL, July 1-3, 1996.

[17]Terhardt, M., Hagemann, G. and Frey, M., *Flow separation and side-load behavior of truncated ideal rocket nozzles*, AIAA 2001-3686, 37th Joint Propulsion Conference, Salt Lake City, UT, July 8-10, 2001.

[18]Vuillermoz, P., Weiland, C., Hagemann, G., Grosdemange, H. and Bigert, M., *Nozzle Design and Optimization*, AIAA Progress in Astronautics and Aeronautics, Vol. 200, Liquid Rocket Thrust Chambers, Chapter 13, pp. 469-492, 2004.

[19]Schmucker, R., *Side Loads and their Reduction in Liquid Rocket Engines*, Rept. TB-14, Technical University of Munich, Bavaria, 1973.

[20]Stark, R. and Génin, C., *Parametrical Study on Side Load Generation in Subscale Rocket Nozzles*, No. 378, EUCASS, 6th European Conference for Aerospace Sciences, Krakw, Poland, June 29 - July 3, 2015.

[21]Génin, C. and Stark, R., *Experimental investigation of cold flow TIC nozzles, a spectral analysis*, AIAA 2016, 52nd Joint Propulsion Conference, Salt Lake City, UT, July 25-27, 2016.

[22]Stark, R. and Génin, C., *Experimental Study on Rocket Nozzle Side Load Reduction*, Journal of Propulsion and Power, Vol. 28, No. 2, pp 307-311, doi: 10.2514/1.58115, 2012.

[23]Stark, R. and Génin, C., *Optimisation of a Rocket Nozzle Side Load Reduction Device*, Journal of Propulsion and Power, in print, 2016.

[24]Stark R., *Beitrag zum Verständnis der Strömungsablösung in Raketendüsen (Contribution to the Understanding of Flow Separation in Rocket Nozzles)*, Ph. D. thesis (in German), RWTH Aachen, 2010.